Nanocomposite films and coatings produced by interaction between graphite oxide and Congo red

**Jurgis Barkauskas · Justina Dakševič · Remigijus Juškėnas ·
Regina Mažeikienė · Gediminas Niaura · Gediminas Račiukaitis ·
Algirdas Selskis · Inga Stankevičienė · Romualdas Trusovas**

Abstract Nanocomposite films and coatings were produced from the aqueous solutions containing different proportions of graphite oxide (GO) and Congo red by filtering through a polycarbonate membrane filter into alkaline media. They were examined by electron microscopy, Raman and FTIR spectroscopy, XRD, contact angle, and electrical conductivity measurements. It was established that the Congo red is able to interact through its amino groups with different functional groups of GO to form larger moieties composed of the nanoplatelets of GO. Raman spectroscopy revealed quinoid-like ring structure for dye adhering to the GO. In the case when the interaction occurs with the terminal functional groups located on the edges of the nanoplateletes of GO, larger crystallites in the nanocomposite are formed. The interaction between the Congo red and functional groups of GO situated in a basal plane leads to more compact structure of the nanocomposite. Pulsed laser treatment was used to reduce GO to graphene. Raman spectra of laser treated areas show positive effect of addition of the Congo red on the graphene yield in nanocomposite coatings after the laser treatment.

J. Barkauskas (✉) · J. Dakševič · R. Juškėnas · A. Selskis ·
I. Stankevičienė
Faculty of Chemistry, Vilnius University, Naugarduko Str. 24,
03225 Vilnius, Lithuania
e-mail: jurgis.barkauskas@chf.vu.lt

R. Mažeikienė · G. Niaura
Institute of Chemistry, Center for Physical Sciences and
Technology, A. Gostauto Str. 9, 01108 Vilnius, Lithuania

G. Račiukaitis · R. Trusovas
Department of Laser Technologies, Center for Physical Sciences
and Technology, Savanoriu Ave. 231, 02300 Vilnius, Lithuania

Introduction

Graphite oxide (GO) is a layered material containing oxygen functional groups on its basal planes and edges. Because of the reactive surface sites and layered structure, it may provide potential nanoscale building blocks for new materials for the synthesis of GO-containing nanocomposites. GO can contain a variety of oxygen functionalities, including both hydroxyl and epoxy groups on the basal planes and carbonyl and carboxyl groups formed on the edges [1–3]. Functional groups are responsible for the hydrophilic properties and dispersibility of GO in water. GO has a layered structure like its precursor graphite, however, the interlayer distance is expanded in comparison with that of the bulk graphite (3.354 Å) and depends on the C/O ratio [4]. The nanoscale sheets of GO are susceptible to the reactions with molecules containing different functional groups. These reactions are used to produce the graphene layers containing a reduced defect density [5, 6]. It has been demonstrated that GO nanocomposites exhibit high mechanical strength combined with exciting physical properties, including tunable electrical and thermal conductivity as well as controlled electron transport [7–11]. While these nanocomposites show a significant improvement in their mechanical properties, they still fall short of the expected theoretical numbers. Overcoming this critical limitation primarily relies on obtaining defect-free sheets of graphene oxide on the one side, and better knowledge of the GO chemistry on the other side.

So far, only a few articles have been devoted to the subject of the interaction between the azo-group and functionalized graphene sheets [12–14]. The interaction results in the increased solubility of carbon nanotubes, graphene sheets, reduced GO, and related carbon nanostructures. Moreover, this type of interaction is used to

produce graphene-based nanocomposites. It is regrettable that the direct interaction between the GO and azo-dyes has rarely been addressed. In this study, interaction between GO and azo-dye Congo red (CR) has been investigated using a number of analytical techniques. Samples containing different GO to CR ratios have been prepared as free-standing films and coatings.

Experimental procedures

GO used in this work was prepared by Hummers method [15] in our laboratory. Obtained brown powder was dried in vacuum to a constant weight and stored in the refrigerator.

GO/CR nanocomposite films and coatings were prepared from aqueous suspensions by filtering through a polycarbonate membrane filter (Milipore; filter diameter 45 mm; pore diameter 0.45 µm) [16]. Obtained GO/CR nanocomposite coatings and films were dried at room temperature, cut-off from the cylinder and used for the further investigations. Coatings and films of various thickness (varying from 600 to 1200 nm) and GO to GR ratio have been prepared. They are marked according to the GO:CR ratio (Table 1).

The samples were treated using a picosecond laser (PL10 100, Ekspla) working at 1064 nm wavelength. Experimental setup included the laser, electro-optical shutter, beam expander, and galvanometric scanner with a focusing objective. During the tests, the average laser power was varied from 30 to 40 mW. Scanning speed was changed in the range 15–30 mm/s. Experiments were conducted with dry (stored in desiccator) nanocomposite coatings in argon atmosphere.

The GO/CR nanocomposite films were analysed with scanning electron microscope (EVO-50 EVP, Carl Zeiss). Contact angle measurements were carried out using a sessile drop method with three-liquid probe. Water, glycerol, and 1-bromonaphthalene were used as reference liquids. A contact angle measurement equipment CAM 200 with computer control and appropriate software was used to measure the static contact angles on the GO/CR nanocomposite coatings. DC conductivity measurements were

performed with a two-electrode probe (Ag electrodes; distance between the electrodes—1.50 mm; electrode parameters—5.00 × 5.00 mm) mounted on a glass plate. Measuring cell was placed in a quartz tube to protect the samples with a nitrogen atmosphere. Agilent 34410A 6½ digital multimeter coupled with a high performance switching system (Omega) controlled by LabView software was used to record the conductivity and temperature data. XRD studies were performed using X-ray diffractometer D8 Advance (Bruker AXS) with Cu Kα radiation, which was separated by a bent multilayer monochromator—Göbel mirror. XRD patterns of films were measured using a grazing incidence method: the angle between the incident parallel beam of X-rays and a sample surface equalled 0.5. Raman measurements were performed with 632.8 nm excitation (He–Ne laser) by using the confocal Raman spectrometer/microscope LabRam HR800 (Horiba Jobin Yvon) equipped with a grating containing 600 grooves/mm and a liquid nitrogen-cooled CCD camera down to −132 °C working temperature. Laser power at the sample was restricted to 1 mW and the laser beam was focused to ∼2 µm diameter spot on the surface. Spectra were taken with 50× objective lens. Measurements performed with lower incident laser power (0.1 mW) showed no spectral change indicating that integrity of the sample was preserved during the Raman experiments. Measurements were carried out in 180° geometry. The integration time was 10 s. Each spectrum was recorded by accumulation of 10 scans yielding overall integration time of 100 s. Raman spectra were captured from different areas of the samples: pristine GO films which were not irradiated by the laser and from the center of laser scribed lines. Raman spectrum of CR in solid state was obtained by FT-Raman spectrometer Spectrum GX (PerkinElmer Inc.) by using 1064 nm (30 mW) laser radiation. Laser beam was focused to ~ 0.2 mm^2 spot on the studied films. Spectral resolution was set to 4 cm^{-1}. Samples used for the FTIR analyses were grounded and pressed with KBr into a tablet. FTIR spectra were recorded using a Perkin-Elmer FTIR Spectrum BXII instrument with a HATR reflectance unit and ZnSe monocrystal. During IR measurements the tablets were placed on the surface of monocrystal and holded by applied vacuum. A background spectrum was run before every sample spectrum. This was subtracted from the sample spectrum.

Results and discussion

Amino-groups situated on the both sides of the CR molecule can react with different functional groups present on the surface of GO sheets in condensation reactions. Together with the direct interaction among functional groups, CR molecules can interact with the GO nanosheets by

Table 1 Percentage of CR in GO/CR nanocomposite samples

Sample	Mass% CR
GO/CR-0	0.00
GO/CR-1	2.27
GO/CR-2	4.44
GO/CR-3	18.87
GO/CR-4	31.75

means of hydrogen bonds, electrostatic Coulomb's forces, and π-stacking interactions. Each type of interaction is specific and temperature dependent. The final result is that the structure and properties of GO/CR nanocomposite coating are dependent on the GO to CR ratio and preparation conditions.

Samples of the GO/CR nanocomposites with various GO to CR ratios were produced both in the form of coatings and films. Coatings obtained on the PC membrane filter were flexible. Free-standing films were stiff and rather brittle when dried but flexible enough in a wet ambient. Mechanical properties of the coatings and films were dependent on the GO to CR ratio; the samples with higher CR content were more flexible and prone to curl. GO/CR coatings and films prepared from non-sonicated aqueous mixtures were more brittle in comparison with those prepared from sonicated mixtures.

SEM images show correlative changes in morphology of the nanocomposite films depending on the GO to CR ratio and the preparation protocol. Top view of the film without CR shows paper-like structure composed of irregularly ordered GO nanosheets. Lateral view demonstrates this paper-like structure more clearly. Paper-like structure is observed in all samples independently on the GO:CR ratio. This kind of morphology suggests that GO filler is dispersed in a CR matrix. Addition of CR to 2.27 % slightly

diminishes wrinkling of the surface of the GO/CR nanocomposite film. Fragment of the fracture shown in Fig. 1b for the sample GO/CR-1 exhibits a denser stacking of GO nanosheets in comparison with the coatings without CR. The further increase in the CR concentration to 4.54 % results in arrangement of the even denser stacking of GO nanosheets (Fig. 1c, d). Ripples observed in the top view SEM image of GO/CR-2 should be a consequence of the closer adherence among the adjacent graphene nanosheets. When concentration of CR is raised to 18.87 %, nanocomposite GO/CR films GO/CR-3 display different morphology (Fig. 1e, f); this time a very fine network of GO ripples is visible. We suggest that observed changes in morphology of GO/CR-3 indicate a deep penetration of CR molecules inside the GO stacks. Morphology of straight intersecting ripples of GO, which reflects the deep CR penetration effect, remains visible in the GO/CR-4 sample with the CR concentration raised to 31.75 % (Fig. 1g, h). However, the same concentration of CR without sonication (Fig. 1i) results in the morphology, which resembles the morphology of GO/CR nanocomposites with ∼7 times lower CR concentration (Fig. 1c). Lateral view of GO/CR-4 (Fig. 1j) reveals a brittle fracture line of the nanocomposite produced without sonication in comparison with the GO/CR film of the same composition produced including the sonication protocol (Fig. 1h). Regular changes in the
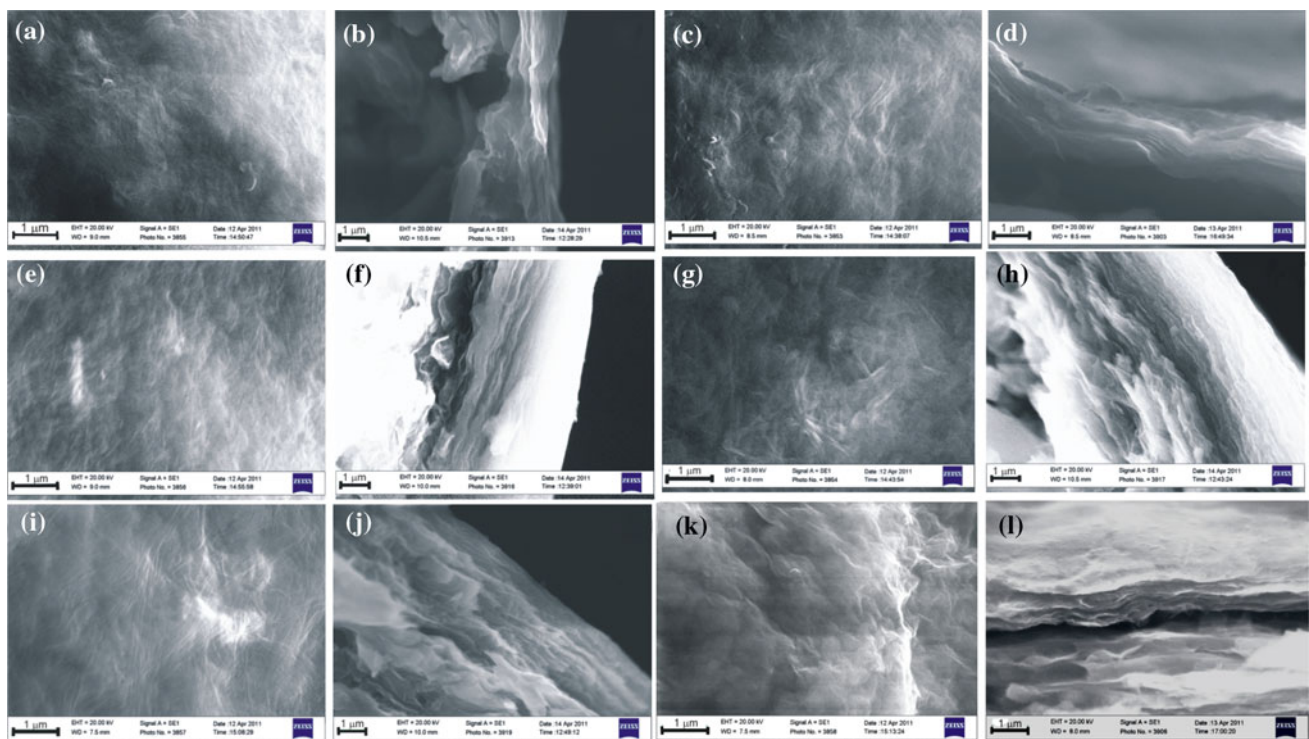

Fig. 1 SEM images of GO/CR nanocomposite films (1.2 μm) obtained at different fraction of CR: **a**, **b** GO/CR-1; **c**, **d** GO/CR-2; **e**, **f** GO/CR-3; **g**, **h** GO/CR-4; **i**, **j** GO/CR-4* (non-sonicated); **k**, **l** GO/ CR-0 (pure GO). Images **a**, **c**, **e**, **g**, **i**, **k** top views; images **b**, **d**, **f**, **h**, **j**, **l** lateral views demonstrating fracture lines

morphology of GO/CR nanocomposite films indicate about a direct interaction between the GO particles and CR molecules and the role of the sonication process to formation of GO/CR nanocomposite structures. Sonication should be able to assist the penetration of CR molecules among the GO stacks.

Contact angle measurements were carried out using a three-liquid probe method based on Lifshitz–van der Waals acid–base theory, which is described in more detail elsewhere [17]. According to this approach it was possible to resolve a total surface energy of a solid (γ_T) into dispersive (γ_D) and polar (γ_P) components, while the latter, in turn, can be resolved into an acidic (γ_A) and a basic (γ_B) part. The dispersive component γ_D theoretically accounts for van der Waals and non-site specific interactions. The polar component γ_P is accounted for the dipole–dipole, dipole-induced dipole, hydrogen bonding, and other site-specific interactions. Acidic γ_A and basic γ_B components refer to the electron-deficient and electron-donating sites on the solid surface, respectively. After measuring the contact angles by using the three-liquid probe method, and introducing the data into a three-variable equation system:

$$\begin{cases} \gamma_T^{L1}(1 + \cos\theta_{L1}) = 2\sqrt{\gamma_D^{L1}\gamma_D^S} + 2\sqrt{\gamma_A^{L1}\gamma_A^S} + 2\sqrt{\gamma_B^{L1}\gamma_B^S} \\ \gamma_T^{L2}(1 + \cos\theta_{L2}) = 2\sqrt{\gamma_D^{L2}\gamma_D^S} + 2\sqrt{\gamma_A^{L2}\gamma_A^S} + 2\sqrt{\gamma_B^{L2}\gamma_B^S} \\ \gamma_T^{L3}(1 + \cos\theta_{L3}) = 2\sqrt{\gamma_D^{L3}\gamma_D^{L3}} + 2\sqrt{\gamma_A^{L3}\gamma_A^{L3}} + 2\sqrt{\gamma_B^{L3}\gamma_B^{L3}} \end{cases}$$
(1)

(here markings L1, L2, and L3 stands for appropriate liquids, and S for solid) it was possible to determine all surface energy components of a solid mentioned above. In our study one non-polar and two polar liquids were used: water ($\gamma_T = 72.80$ mJ/m^2; $\gamma_D = 21.80$ mJ/m^2; $\gamma_A = 25.00$ mJ/m^2; $\gamma_B = 25.00$ mJ/m^2), glycerol ($\gamma_T = 64.00$ mJ/m^2; $\gamma_D = 34.00$ mJ/m^2; $\gamma_A = 3.92$ mJ/m^2; $\gamma_B = 57.40$ mJ/m^2), and 1-bromonaphthalene ($\gamma_T = 44.40$ mJ/m^2; $\gamma_D = 44.40$ mJ/m^2; $\gamma_A = 0.00$ mJ/m^2; $\gamma_B = 0.00$ mJ/m^2) [18]. Data on the surface energy components and their dependence on the amount of CR in GO/CR nanocomposite coatings are presented in Fig. 2a.

Total surface energy determined for the coatings GO/CR-0 (thickness 600 nm) composed of pure GO equals 63 mJ/m^2; this result is in a good correspondence with the reports elsewhere [19]. This energy consists of both dispersive ($\gamma_D = 42.7$ mJ/m^2) and polar ($\gamma_P = 20.3$ mJ/m^2) contributions, while the major component in polar surface energy are the acidic surface sites ($\gamma_A = 69.2$ mJ/m^2). Addition of CR to the GO/CR nanocomposite coatings leads to a 30 % decrease of the total surface energy ($\gamma_T = 45$ mJ/m^2); this result is closer to the surface energy reported for graphene [19]. Most probably, observed shift
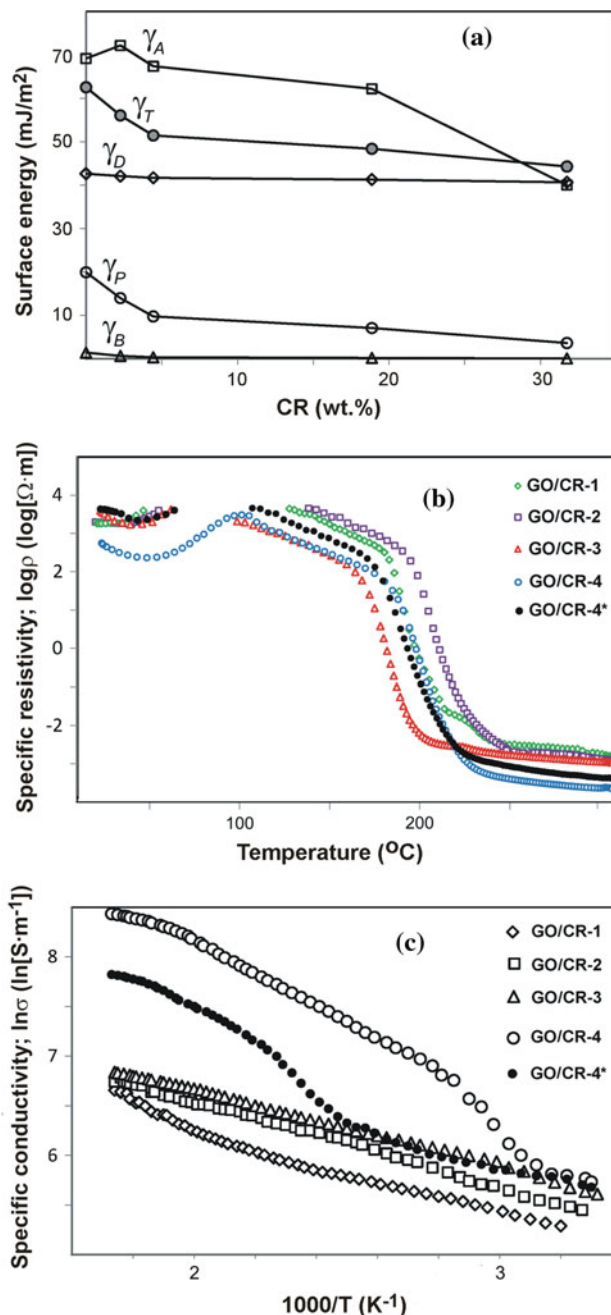

Fig. 2 Contact angle and conductivity measurements: **a** Surface energy dependence on the CR amount in GO/CR nanocomposite coatings (600 nm thickness). **b** Variations in specific resistance of GO/CR nanocomposite (logarithmic scale) with temperature increase. **c** Dependences of specific conductivity (logarithmic scale) of annealed GO/CR nanocomposite samples on reciprocal temperature

is related to the structural changes during the formation of the more compact GO/CR nanocomposite specimens containing higher amounts of CR (see Fig. 1). Dispersive component, γ_D, is not sensitive to the addition of CR, while the polar component, γ_P, decreases to 3.6 mJ/m^2, for the GO/CR-4 with 31.75 wt% CR content in the

nanocomposite. Simultaneously, input of acidic sites decreases to 40 mJ/m². Knowing that a surface energy should be directly proportional to the surface area, all the facts mentioned above lead us to conclude that adsorption of CR may occur predominantly either on the edges or between the basal planes of GO. CR molecules, being incorporated between the basal planes, are able to reduce the γ_A values by increasing electron density in the single layer of GO. In this case, sulfo-groups attached to the both sides of the CR molecule, do not interact directly with the active sites on the GO surface and are not sufficient to increase its acidity.

GO/CR nanocomposites are composed of two phases with different electro-conductive properties: GO, which is a semiconductor, and CR, being an electrical insulator. At higher temperatures GO undergoes a process of thermal reduction and restoration of π-electron system of graphene [20]. In the case of at least one of the phases in the nanocomposite being electrically conducting, electrical resistance measurements can be used to study the structure of nanocomposite. Resistance measurements are quick, involve relatively simple equipment, and tend to give general information on the nanocomposite structure. In our study two sets of resistance measurements were performed. In one series of measurements, carried out at non-equilibrium conditions, resistance data were recorded by raising the temperature at a rate of 5 deg/min to 300 °C. Another series of measurements was carried out at equilibrium conditions by measuring electrical resistance of GO/CR nanocomposite films annealed at 300 °C. Results of both series of measurements are presented in Fig. 2b, c, respectively. Samples for the resistance measurements were prepared in form of films of 1200 nm thickness.

Results obtained at non-equilibrium conditions represent structural changes in GO/CR nanocomposite samples by increasing the temperature. At room temperature all samples are characterized by high resistance values (~ 1 GΩ), which lie near the instrument measuring range. Resistance values of GO/CR-0 film made of pure GO (without addition of CR) exceeded upper measuring limits. These observations confirm the conclusion drawn through SEM analysis about the formation of more compact structure of GO/CR nanocomposite with addition of CR. The highest degree of compactness is reached for GO/CR-4, the sonicated GO/CR films containing 31.75 wt% of CR, while for the GO/CR-4*, non-sonicated ones with the same GO/CR ratio, resistance values are comparable with the samples having considerably smaller quantities of CR. Shape of resistance curves obtained at higher temperatures consists of three linear segments, which are similar for all GO/CR nanocomposite samples. It reflects the structural changes in the GO/CR nanocomposite matrix, especially the formation of new conducting interphases during the raise of the temperature. The slopes within each segment are approximately uniform, regardless the composition of a sample. Such uniformity suggests that the major contribution to the formation of conducting phase should be obtained from the thermal decomposition of GO. Variations observed in Fig. 2b include either the absolute values of resistivity or the temperature intervals of each segment. The values of slopes in each segment are directly proportional to the rate of formation of electroconducting phase and the deviation of the system from equilibrium. They show that the most prompt formation of electroconducting phase (up to 0.16 log[Ω·m]/deg) is observed in the temperature range of 180–230 °C, depending on the composition of a sample. Obtained results demonstrate that the stage including this temperature interval is the most sensitive in formation of the electroconductive phase. Series of further experiments are planned to explore in more detail the transformations that occur in the GO/CR nanocomposites in this temperature interval and at higher temperatures as well.

In the temperature region of 200–250 °C, the rate of electroconductive phase formation sharply drops to below 0.007 log[Ω·m]/deg, and specific resistivity reaches the values, which are comparable to those referred for graphite in basal plane [21]. Samples with highest CR content (sonicated and non-sonicated ones; GO/CR-4 and GO/CR-4*, respectively) at 300 °C attain lower (~ 10 times) resistance values in comparison to the samples with lower CR content. Therefore, it can be concluded that CR molecules can act as curable agents in formation of the graphene structure. One may suppose that the bridges emerged during the condensation reactions between GO sheets through the skeletons of CR molecules, are sufficiently short to allow an electron tunneling between the new-formed conducting graphene nanoplatelets. We intend that a more comprehensive understanding of this process will be achieved in our future studies which will be accomplished by using an extended range of curing agents with the molecular structure similar to that of CR.

Resistance measurements carried out on annealed GO/CR nanocomposites at equilibrium conditions were used to study the electron migration in the new-formed conducting phases. In Fig. 2c the plots of ln σ versus $1/T$ are linear within particular temperature intervals. Without going much into details, the slopes of these plots represent the energy barriers for electron migration (E_{migr}) between the nanoplatelets of conductive phase [22]. Values of E_{migr} determined for annealed GO/CR nanocomposite samples (Table 2) lie in the range of 60–130 meV, and are consistent with the data obtained by other authors [23–25]. The change of slopes at higher temperatures for the samples GO/CR-4 and GO/CR-4* (sonicated and non-sonicated ones; containing 31.75 wt% of CR), indicates different electron transport pathways, which occur with altered

Table 2 Energy of electron migration (E_{migr}) and XRD data for GO/CR nanocomposite samples

Sample	E_{migr} (meV)	Reflection angle, 2θ	Interplanar distance (Å)	Crystallite size (nm)
GO/CR-0	–	11.038	8.009	7.97
GO/CR-1	78.3	11.033	8.013	9.57
GO/CR-2	74.7	10.996	8.040	11.49
GO/CR-3	66.2	10.862	8.139	9.78
GO/CR-4	69.6; 129.0[b]	10.899	8.112	7.64
GO/CR-4[a]	64.4; 125.6[b]	10.779	8.202	8.68

[a] Non-sonicated sample

[b] Values obtained at higher temperatures (see Fig. 4)

conditions. More detailed study of this process will be conducted in the future.

GO/CR nanocomposite coatings of 600 nm thickness were examined using a grazing incidence X-ray diffraction method. The XRD results are shown in Fig. 3a and summarized in Table 2. Inlet in Fig. 3a demonstrates shape of the XRD peaks at $2\theta \approx 11°$ in more details.

XRD analysis show that GO/CR nanocomposite samples obtained using different GO to CR ratios have different structural characteristics. Interplanar distances gradually increase with increasing CR portion in the nanocomposite. It may be assumed that the CR molecules are able to replace the water molecules from the interplanar space of GO sheets. The procedure of sonication promotes the direct
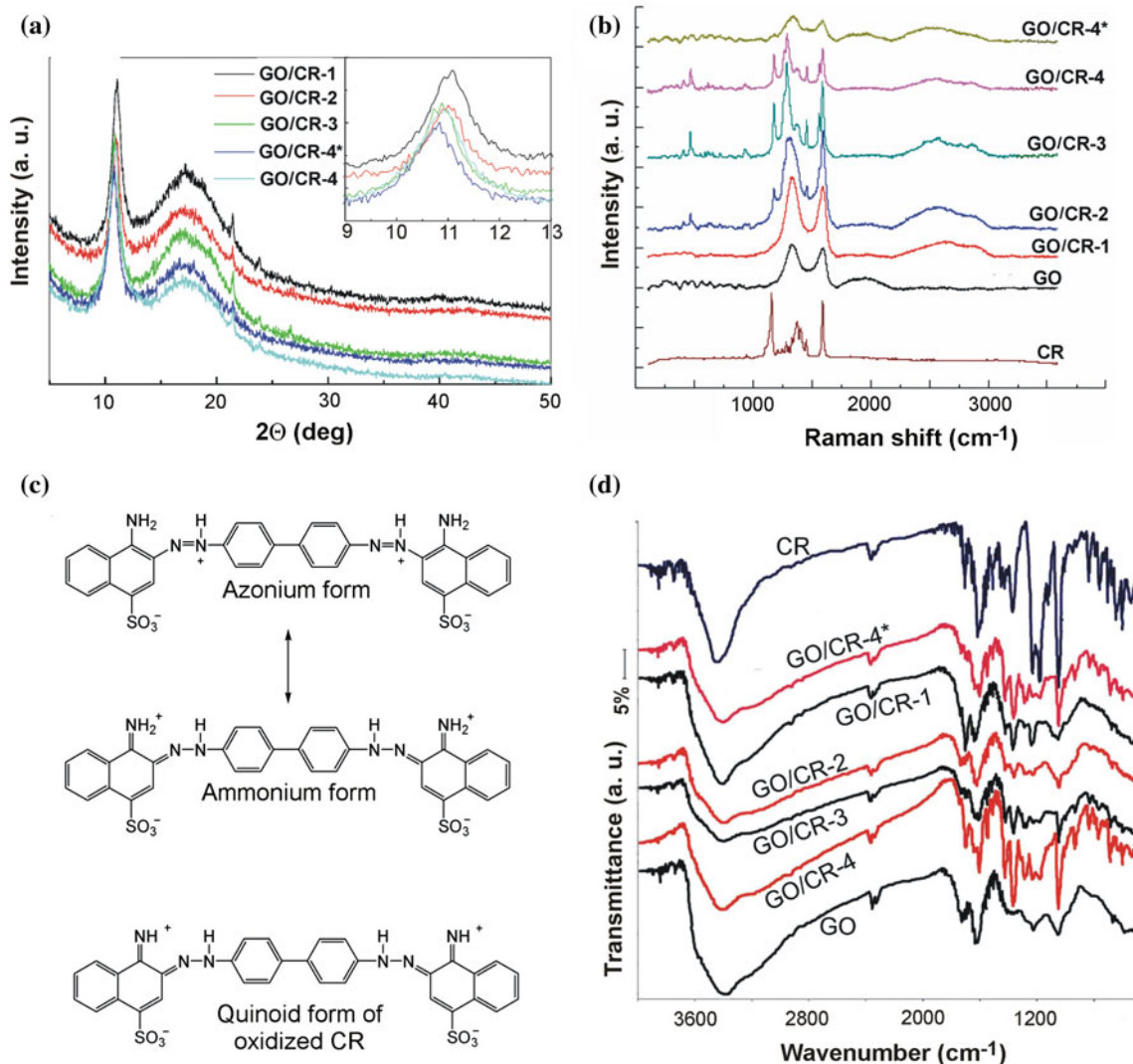

Fig. 3 a XRD patterns of GO/CR nanocomposite coatings (thickness of 600 nm). **b** Raman spectra of GO, CR, and their nanocomposite mixtures. **c** Two resonance structures (azonium and ammonium) of protonated CR and quinoid structure of $2e^-$ oxidation product of CR [27]. **d** FTIR spectra of GO, CR, and GO/CR nanocomposite samples (* stands for the samples prepared from non-sonicated mixture)

interaction between the GO functional groups and CR molecules; therefore, interplanar distance in the sonicated sample GO/CR-4 is less comparing with the non-sonicated one sample GO/CR-4*. The size of crystallites runs through a maximum with increasing the portion of CR in the nanocomposites. Small amounts of CR (up to 4.5 %) act positively on the formation of the larger crystallites, while the more significant portions of CR act in the opposite direction. We can consider that CR molecules interacting primarily with the functional groups attached to the edges of GO sheets are able to combine them into the larger units.

Raman spectra of the GO/CR nanocomposite coatings (600 nm thickness) together with the spectra of pure GO and CR are presented in Fig. 3b. Two main peaks assigned to G (1580 cm^{-1}) and D bands (1310–1430 cm^{-1}), which are E_{2g} vibrational mode in-plane and A_{1g} breathing mode, respectively, are prominent in the GO and GO/CR nanocomposite samples [26]. With increasing CR proportion in the nanocomposite, Raman bands called 2D and D + G, located at 2700–3000 cm^{-1}, appear. 2D band is Raman active for crystalline graphitic materials and it is sensitive to the π band in the graphitic electronic structure, while the combination mode of D + G is induced by disorder [26]. Our result indicates that due to the increased intensity of 2D band in Raman spectra, the size of sp^2 domains is increased after addition of small amounts of CR (up to 4.5 %). Excess of CR tends to reduce the intensity of 2D and D + G Raman bands. These observations are consistent with the results obtained after examining XRD spectra of the GO/CR nanocomposite samples.

Analysis of Raman spectrum of CR provides possibility to elucidate the structure of the dye in the GO/CR nanocomposites. Positions of the characteristic Raman bands of CR in various forms and assignment of the bands based on previous studies [27–29] are provided in Table 3. Frequencies of the CR in the complex GO–CR differ considerably as comparing with spectrum of the dye in the solid state. In particular, the v(phenyl-N) mode frequency increases from 1156 to 1176 cm^{-1}, indicating strengthening of the phenyl-N bond.

Such increase in bonding order between the phenyl ring and azo moiety is consistent with the ammonium (quinoid) resonance structure of protonated CR presented in Fig. 3c. Frequencies of other characteristic vibrational modes are also consistent with protonated dye form (Table 3). It should be noted, that vibrational spectrum of CR in protonated state (ammonium resonance structure) is very similar to previously observe oxidized CR form (Fig. 3c), therefore cannot be unambiguously distinguished by Raman spectroscopy [27].

In Fig. 3d the FTIR spectra of GO, CR, and CR–GO mixtures are presented. FTIR spectrum of GO sample is

Table 3 Comparison of Raman bands (cm^{-1}) for the CR in various states and assignments

Solid state CR	Protonated form[a] (CRH_2)	Oxidized form[a]	CR–GO[b]	Assignment[c]
1156	1180	1176	1176	v(phenyl-N)
1280	1289	1287	1286	v(phenyl–phenyl)
1353	1372	1373	1368	v(naphthyl)
1405	–	–	–	v(N=N)
1452	1455	1456	1454	v(N=N)
–	1562	1562	1560	
1592	1593	1593	1590	v(phenyl)

[a] From Ref. [27], [b] from spectrum of sample GO/CR-3, [c] based on Refs. [27–29]

consistent with the spectra reported elsewhere [30, 31]. The most characteristic features are broad intense band at 3400 cm^{-1} (O–H stretching vibrations) and the bands at 1730 cm^{-1} (C=O stretching vibrations from carbonyl and carboxyl groups), 1560 cm^{-1} (skeletal vibrations from unoxidized graphitic domains), 1226 cm^{-1} (C–OH stretching vibrations), and 1055 cm^{-1} (C–O–C stretching vibrations).

The broad and strong absorption band near 3450 cm^{-1} in the FTIR spectrum of solid state CR is associated with the stretching vibration of N–H bonds [12, 32–34]. The absorption near 1595 cm^{-1} was assigned to stretching vibration of –N=N– bond, while the bands at 1364 and 1227 cm^{-1} might be associated with the stretching vibrations of =C–N= group adjacent to aromatic ring. Several low frequency absorption bands located at 832, 757, and 697 cm^{-1} are characteristic for aromatic rings C–H out-of-plane deformation modes [34]. In contrast to Raman scattering, FTIR spectrum clearly shows vibrations of -SO₃ group, which are located at 1178 and 1047 cm^{-1} [12, 33, 34]. Appropriate changes in the FTIR spectra of CR–GO mixtures with different quantities of CR are apparent. The band at 1047 cm^{-1}, representing sulfonate group, keeps unchanged position and have a tendency to increase with increasing the ratio of CR. From this it can be concluded that the sulfonate functional group do not interact with GO nanoparticles during the adsorption process. The same conclusion is made from the contact angle measurements. Transformations of different type are observed in the region of bands representing vibrations of nitrogen atom. The band at 1364 cm^{-1} appears in GO–CR mixtures at minimal ratio of CR, while height of the peak at 1227 cm^{-1} is much less in comparison with the peak in the spectrum of pure CR and the shape of the peak is changed. The new absorption band appears at 1420 cm^{-1} indicating changes in CR structure comparing with solid state spectrum, which is consistent with the resonant Raman studies. The broad band at 3450 cm^{-1} representing N–H stretching vibrations is shifted down to the region of 3400 cm^{-1}. Such changes suggest

involvement of N–H groups into interaction with GO. The band representing characteristic C–O–C vibrations at 1055 cm^{-1} disappears at higher ratios of CR. The band of GO at 1226 cm^{-1} (C–OH stretching vibrations) is likely covered by the band of CR at 1227 cm^{-1} (=C–N= stretching vibrations). The features of GO FTIR spectrum are gradually changed in the CR–GO mixtures. The band at 1730 cm^{-1} (C=O stretching vibration) gradually decreases with increasing the ratio of CR except for the sample GO–CR-1 with the minimum ratio of CR, indicating transformation of carbonyl or carboxyl groups of GO due to the interaction with ammonium groups of dye molecules. Such interaction is supported by the changes in N–H stretching region.

GO is a good precursor for graphene formation. Treatment with a laser beam can be used for local reduction of GO to graphene [35–37]. We applied picosecond laser irradiation to GO/CR nanocomposite coatings (thickness 1200 nm) with different CR concentration. Mean laser power and scanning speed were varied to find out the optimal irradiation conditions for graphene phase formation. The laser treatment was performed in argon ambient to prevent oxygen effect from the air. The laser treated areas of the samples were investigated by Raman spectroscopy. The intensity ratio for Raman lines D ($\sim$1320 cm^{-1}), G ($\sim$1580 cm^{-1}), and 2D ($\sim$2700 cm^{-1}) are often used as criterion of the graphene phase quality [38–45]. Minimum of I_D/I_G and maximum of I_{2D}/I_G corresponds to highest quality of the graphene and in our case the optimal conditions for GO-to-graphene reduction. Because D-band appears due to disorder in the sp^2-network, the intensity ratio I_D/I_G sharply decreases with decreasing the density of defects in graphene [40]. On the other hand, the ratio I_{2D}/I_G probes the integral numbers of graphene layers per film, increasing up to $\sim$4 for a single graphene layer [39, 41].

The absolute best results in our experiments were obtained when laser power was 40 mW and scanning speed was 25 mm/s. Raman spectrum of laser proceed area of GO/CR nanocomposite with the CR concentration 18.87 wt% is shown in Fig. 4a.

Presence of intense 2D feature indicates formation of graphene-like structure due to the laser treatment of GO/CR film. The frequency of symmetric 2D band (2660 cm^{-1}) coincides well with the estimated value for a single layer graphene [46]. This band was approximated by Lorentzian form and the band width estimated as full width at half maximum (FWHM) was found to be 55 cm^{-1}. Estimated value is about two times higher as expected for perfect single graphene layer [39]. Relatively low I_{2D}/I_G ratio and intense D band indicates presence of defects and the structure composed of several graphene layers. Ratio of the intensities of the Raman lines depends on the CR concentration. Figure 4b presents results variation in I_D/I_G and I_{2D}/I_G depending on the CR concentration in nanocomposites treated with the
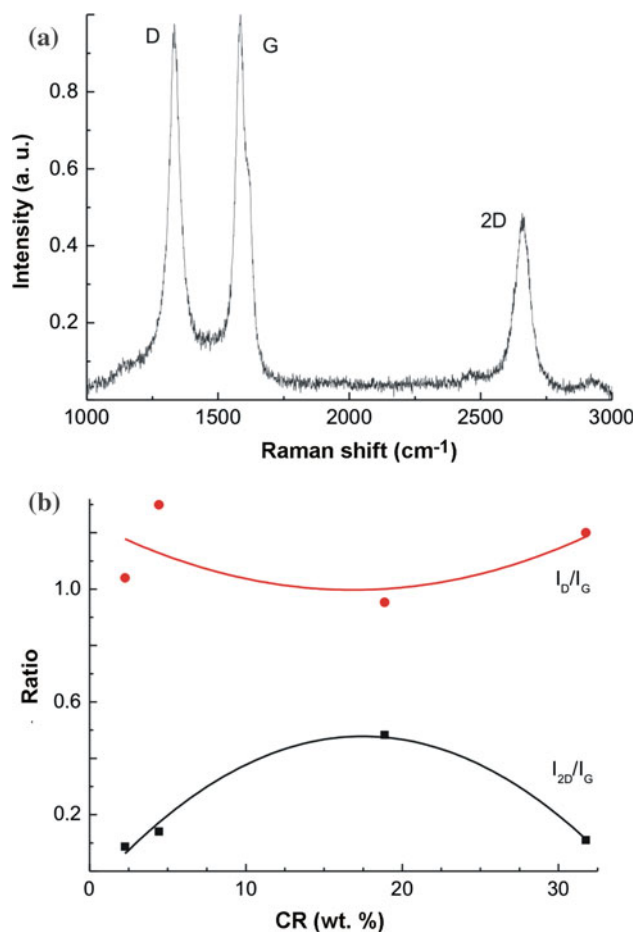

Fig. 4 **a** Raman spectrum of laser treated GO/CR nanocomposite (GO/CR-3). **b** Dependence of intensities ratio of Raman lines D, G, and 2D on the CR concentration in laser treated GO/CR nanocomposite. Laser process parameter: wavelength 1064 nm; mean laser power 40 mW, scanning speed 25 mm/s

laser at identical conditions. Variation in the intensities ratios related to quality of resulting graphene film indicate importance of the CR concentration on linkage of graphene sheets together and formation larger blocks with increase in order. Existence of the optimal GO to CR ratio in GO/CR nanocomposites is consistent with conductivity, XRD, and Raman measurements performed in this work.

Conclusion

GO/CR nanocomposite coatings and films have been prepared by slow filtering an aqueous dispersion of GO and CR mixture through the polycarbonate membrane filter into alkaline solution. GO/CR coatings prepared on the polycarbonate substrate were flexible, while the GO/CR films were brittle when dry but flexible enough in a wet ambient. The coatings and films were examined by SEM and XRD technique, Raman, and FTIR spectrometry, the contact

angle, and conductivity measurements. GO/CR nanocomposite coatings have been treated by laser and analyzed using a Raman spectroscopy and SEM. It was estimated that sonication procedure was able to assist penetration of CR molecules among the GO stacks to form a compact structure composed of GO nanoplatelets. Annealing of GO/CR samples to 300 °C increased the conductivity of the nanocomposite films about 10^9 times, reaching the values, which are comparable to the conductivity of graphite basal plane. XRD, Raman, and FTIR measurements show that amino groups in the CR molecule were able to interact with functional groups of GO, while sulfo groups tended not to react. Raman analysis revealed quinoid-like structure of CR dye in the GO/CR complex. According to our experiment data, the reaction between GO and CR can occur in two distinct ways. At lower CR concentration prevails the interaction between the amino groups in CR molecule and the functional groups of GO located on the edges of nanoplatelets. This reaction leads to the formation of the larger moieties of GO crystallites. At higher concentration majority of CR molecules are able to penetrate between the stacks of GO nanoplatelets and interact with the epoxy- and hydroxyl-functional groups situated in the basal planes to form the more compact structure of nanocomposite. Investigations of laser treatment of GO/CR nanocomposite coatings in order to reduce them into graphene structure revealed an optimal CR concentration when the best quality of graphene can be locally achieved in the coatings. The concentration corresponds to the situation where CR molecules preferentially are located on the edges of GO sheets and join them together, creating the larger nanoplatelets.

References

1. Dreyer DR, Park S, Bielawski CW, Ruoff RS (2010) Chem Soc Rev 39:228
2. Rourke JP, Pandey PA, Moore JJ, Bates M, Kinloch IA, Young RJ, Wilson NR (2011) Angew Chem Int Ed 50:3173
3. Wilson NR, Pandey PA, Beanland R, Young RJ, Kinloch IA, Gong L, Liu Z, Suenaga K, Rourke JP, York SJ, Sloan J (2009) ACS Nano 3:2547
4. Wang H, Hu YH (2011) Ind. Eng. Chem. Res. 50:6132
5. Datta S, Htet M, Webster DC (2011) Macromol Mater Eng 296:70
6. Zhu YW, Murali S, Cai WW, Li X, Suk JW, Potts JR, Ruoff RS (2010) Adv Mater 22:3906
7. Chen H, Muller MB, Gilmore KJ, Wallace GG, Li D (2008) Adv Mater 20:3557
8. Chen C, Yang Q, Yang Y, Lv W, Wen Y, Hou P, Wang M, Cheng H (2009) Adv Mater 21:3007
9. Park S, Dikin DA, Nguyen ST, Ruoff RS (2009) J Phys Chem C 113:15801
10. Rafiee MA, Rafiee J, Wang Z, Song H, Yu Z, Koratkar N (2009) ACS Nano 3:3884
11. Dikin DA, Stankovich S, Zimney EJ, Piner RD, Dommett GHB, Evmenenko G, Nguyen ST, Ruoff RS (2007) Nature 448:457
12. Li FH, Bao Y, Chai J, Zhang Q, Han D, Niu L (2010) Langmuir 26:12314
13. Rao CNR, Sood AK, Subrahmanyam KS, Govindaraj A (2009) Angew Chem Int Ed 48:7752
14. Hu CG, Hu SS (2008) Langmuir 24:8890
15. Hummers WS, Offeman RE (1958) J Am Chem Soc 80:1339
16. Barkauskas J, Stankevičienė I, Dakševič J, Padarauskas A (2011) Carbon 49:5373
17. Dwari RK, Hanumantha Rao K, Somasundaran P (2009) Int J Miner Process 91:100
18. Janczuk B, Bialopiotrowicz T, Zdziennicka A (1999) J Colloid Interface Sci 211:96
19. Mukhopadhyay P, Gupta RK (2011) Plast Eng 67:32
20. Mattevi C, Eda G, Agnoli S, Miller S, Mkhoyan KA, Celik OM, Mastrogiovanni D, Granozzi G, Garfunkel E, Chhowalla M (2009) Adv Funct Mater 19:1
21. Shao Q, Liu G, Teweldebrhan D, Balandin AA (2008) Appl Phys Lett 92:202108
22. Eda G, Chhowalla M (2009) Nano Lett 9:814
23. Trushin M, Schliemann J (2007) Phys Rev Lett 99:216602
24. Chua LL, Wang S, Chia PJ, Chen L, Zhao LH, Chen W, Wee ATS, Ho PKH (2008) J Chem Phys 129:114702
25. Xia F, Farmer DB, Lin Y, Avouris P (2010) Nano Lett 10:715
26. Zhan D, Ni Z, Chen W, Sun L, Luo Z, Lai L, Yu T, Thye A, Wee S, Shen Z (2011) Carbon 49:1362
27. Bonancea CE, do Nascimento GM, de Souza ML, Temperini MLA, Corio P (2006) Appl Catal B 69:34
28. Elhaddaoui A, Merlin JC, Delacourte A, Turrell S (1992) J Mol Struct 267:113
29. Cooper TM, Stone MO (1998) Langmuir 14:6662
30. Ren PG, Yan DX, Ji X, Chen T, Li ZM (2011) Nanotechnology 22:055705
31. Paredes JI, Villar-Rodil S, Martınez-Alonso A, Tascon JMD (2008) Langmuir 24:10560
32. Hu C, Chen Z, Shen A, Shen X, Li J, Hu S (2006) Carbon 44:428
33. Wang L, Wang A (2008) J Hazard Mater 160:173
34. Socrates G (2001) Infrared and Raman characteristic group frequencies, 3rd edn. Wiley, Chichester
35. Cappelli E, Orlando S (2007) J Phys: Conf Series 59:616
36. Zhou Y, Bao Q, Varghese B, Tang LAL, Tan CK, Sow CH, Loh KP (2010) Adv Mater 22:67
37. Trusovas R, Račiukaitis G, Barkauskas J, Mažeikienė R (2011) In: Proceddings of 12th international symposium on laser precision microfabrication (LPM2011), Takamatsu, Japan, June 7–10
38. Lee J, Shim S, Kim B, Shin HS (2011) Chem Eur J 17:2381
39. Gupta A, Chen G, Joshi P, Tadigadapa S, Eklund PC (2006) Nano Lett 6:2667
40. Lucchese MM, Stavale F, Ferreira EHM, Vilani C, Moutinho MVO, Capaz RB, Achete CA, Jorio A (2010) Carbon 48:1592
41. Ferrari AC, Meyer JC, Scardaci V, Casiraghi C, Lazzeri M, Mauri F, Piscanec S, Jiang D, Novoselov KS, Roth S, Geim AK (2006) Phys Rev Lett 97:187401
42. Calizo I, Bao W, Miao F, Lau CN, Balandin AA (2007) Appl Phys Lett 91:201904
43. Calizo I, Miao F, Bao W, Lau CN, Balandin AA (2007) Appl Phys Lett 91:071913
44. Calizo I, Bejenari I, Rahman M, Liu G, Balandin AA (2009) J Appl Phys 106:043509
45. Parvizi F, Teweldebrhan D, Ghosh S, Calizo I, Balandin AA, Zhu H, Abbaschian R (2008) Micro Nano Lett 3:29
46. Amini S, Garay J, Liu G, Balandin AA, Abbaschian R (2010) J Appl Phys 108:094321